

A Piecewise Potential Vorticity Inversion Algorithm and Its Application to Hurricane Inner-Core Anomalies

CHANH Q. KIEU

Department of Meteorology, The Pennsylvania State University, University Park, Pennsylvania

DA-LIN ZHANG

Department of Atmospheric and Oceanic Science, University of Maryland, College Park, College Park, Maryland

(Manuscript received 22 December 2009, in final form 7 March 2010)

ABSTRACT

In this study, a piecewise potential vorticity (PV) inversion algorithm for an arbitrary number of PV pieces is developed by extending Wang and Zhang's PV inversion scheme, and then the nonlinear responses to various types and magnitudes of axisymmetric PV anomalies (PVAs) in hurricane vortices are investigated. Results show that the upper- and lower-level PVAs in the eye help enhance cyclonic flows in the eyewall, but with weak vertical interactions between them. The balanced flows corresponding to the PVAs in the eyewall appear to account for a substantial portion of the warm core and the minimum pressure in the eye. However, the lower-level PVA in the eye inversion layer is more effective in contributing to the hurricane intensity than that at the upper levels. Results also show that the radius of the balanced response of PVAs is more sensitive to the mean vortex intensity than the vertical penetration; the weaker the mean vortex intensity, the larger the radius of the influence will be. Similar behaviors are also observed for the quasi-balanced secondary circulations. That is, given a diabatic heating profile in the eyewall, the weaker the background vortex or the PVAs, the stronger the secondary circulations will be.

It is found that the development of an outer eyewall (or spiral rainbands) could be inimical to the inner eyewall in several ways, such as by 1) adding an anticyclonic flow inside to offset the cyclonic rotation of the inner eyewall, 2) enhancing a ring of a lower pressure zone underneath to broaden the inner-core lower pressure region, 3) inducing an inward (outward) radial flow outside (inside) in the PBL (upper level) to block the energy supply to (outflow of) the inner eyewall, and 4) generating subsidence between the two eyewalls to suppress the development of deep convection in the inner eyewall.

1. Introduction

Potential vorticity (PV) has long been recognized as a powerful and succinct quantity since its first introduction by Rossby (1940). It was used early as a tracer of air masses, and later as a dynamical variable to study the three-dimensional (3D) balanced flows under the invertibility principle; see Hoskins et al. (1985, hereafter HRM) for a comprehensive review. One important characteristic of PV is that once generated it could be preserved for a period of time in the absence of friction and diabatic heating, especially above the planetary boundary layer (PBL). In particular, the migration of PV anomalies

(PVAs) from one region to another tends to induce balanced responses of the mass and wind fields at their vicinities, leading to the development or enhancement of atmospheric disturbances.

High PV¹ and PVA are always present in hurricanes because of the rapid release of latent heat in the eyewall and spiral rainbands and the radial eddy mixing of PV. They propagate three-dimensionally, often in connection to the rapid intensification of hurricanes and their structural changes (Guinn and Schubert 1993; Yau et al. 2004; Chen and Yau 2001). An example of the vertical cross section of PV for a typical hurricane system is given in Fig. 1 (see Yau et al. 2004), showing the axisymmetric

Corresponding author address: Dr. Da-Lin Zhang, Department of Atmospheric and Oceanic Science, University of Maryland, College Park, College Park, MD 20742.
E-mail: dalin@atmos.umd.edu

¹ For the sake of our discussion, we have assumed that PV in the environment is negligible compared to the magnitude of PV in hurricanes, except in the stratosphere.

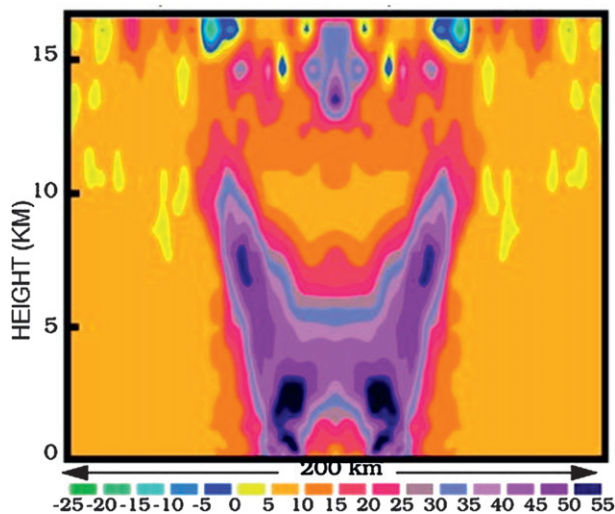


FIG. 1. Vertical cross section of (azimuthally averaged) PV (shaded at intervals of 5 PVU) through the center of Hurricane Andrew (1998) from a cloud-resolving simulation with the finest grid size of 2 km. From Yau et al. (2004).

distribution of high PV values [e.g., >55 PV units (PVU); $1 \text{ PVU} = 10^{-6} \text{ m}^2 \text{ K kg}^{-1} \text{ s}^{-1}$] in the eyewall and shallow layers of high PV (e.g., 30–40 PVU) near the top of the PBL and near the tropopause, both in the eye where the static stability is large. Although these features are from a cloud-resolving simulation, they are believed to be realistic, considering that today's hurricane models have been shown to be capable of reproducing many observed features in hurricanes (e.g., Liu et al. 1999) and other mesoscale convective systems (MCSs). For example, a recent observational study of Bell and Montgomery (2008) exhibits the vertical PV distribution of Hurricane Isabel (2003) during its mature stage that is very similar to that shown in Fig. 1, with a PV bridge in the inner-core region right above the PBL. Similar vertical PV structures have also been seen from our simulations of Hurricanes Bonnie (1998) and Wilma (2005) (not shown). Evidently, all the PV entities shown in Fig. 1 may contribute collectively to the total intensity and 3D structures of the hurricane's rotational flows. However, little is known as to what proportion in magnitude and to what extent in space each PV entity contributes to the hurricane intensity and its total flows.

Previous observations have also shown one or more episodes of distinct spiral rainbands that wrap around an inner eyewall and form a pattern of double concentric eyewalls during the rapid intensification of hurricanes (Willoughby et al. 1982, 1984; Black and Willoughby 1992; Blackwell 2000; Wang 2009). These outer convective rings are kept well separated from the inner eyewall by a moat area, and their formation often leads to hurricane intensity fluctuations. However, such a concentric

configuration appears to be unstable and it is commonly accompanied by replacement processes in which the outer eyewall contracts and intensifies whereas the inner eyewall gradually collapses. The outer eyewall can be characterized not only by strong radar reflectivity but also by a secondary maximum of tangential winds and high PV (Willoughby et al. 1982; Blackwell 2000; Kossin et al. 2000; Chen and Yau 2001; McNoldy 2004; Zhu et al. 2004; Rozoff et al. 2008). It has been hypothesized that the outer eyewall acts as a shield preventing the inflow of saturated air in the PBL and tends to induce subsidence suppressing the development of deep convection in the inner eyewall (see Black and Willoughby 1992; Wang 2008). While this induced subsidence is important in its own right in causing the inner eyewall to collapse, other dynamical roles of the outer eyewall during the replacement processes are still not well understood. Using an idealized balanced model, Rozoff et al. (2008) confirm that the outer eyewall could indeed induce subsidence to the inner eyewall, but its magnitude is so weak that the subsidence would not play any significant role in the dissipation of the inner eyewall. As their analysis is only applied to a barotropic vortex with a radial constant static stability, such hypothetical subsidence by the outer eyewall remains to be validated with sound approaches and realistic hurricane-like vortices.

The objectives of this study are to a) extend the PV inversion algorithm of Wang and Zhang (2003, hereafter WZ03) from one PV piece to multiple PV piece applications and then b) examine the dynamical effects of the above-mentioned axisymmetric PVAs on the intensity and structures of hurricane vortices using the piecewise PV inversion algorithm. This will be done by treating PV rings in the outer eyewall and the inner eyewall as well as the upper and lower PV core as separate PV pieces and then using the piecewise inversion to investigate their corresponding balanced mass and wind fields. In other words, given a PVA, we attempt to examine how its corresponding balanced perturbations will be distributed and what their magnitudes are *in a highly rotational background*.

The next section provides a literature review of piecewise PV inversion algorithms and their related applications. An extension of WZ03's PV inversion of one piece to multiple pieces will be discussed. Section 3 presents a new algorithm that allows for effectively solving the piecewise PV inversion with an arbitrary number of pieces. Section 4 shows the balanced flows corresponding to various PVA pieces in an idealized hurricane vortex at different intensities. Section 5 addresses the dynamic and thermodynamic roles of the outer eyewall during the eyewall replacement cycle. A summary and concluding remarks are given in the final section.

2. Review

Following the seminal work of HRM, Davis and Emanuel (1991, hereafter DE91) and Davis (1992) developed a piecewise PV inversion algorithm to obtain nonlinear balanced (NLB) flows associated with different types of PVAs. This algorithm has proven to be useful in many mesoscale applications for which the Rossby number associated with the divergent flows is reasonably small compared to that associated with the rotational flows. For example, Wu and Emanuel (1995a,b) use it to show the importance of large-scale environmental PVAs in determining the movements of hurricanes. Huo et al. (1998, 1999) apply it to improving the model initial conditions with the oceanic surface observations for the prediction of an intense winter storm, and studying the effects of the upper-level merging troughs on the rapid deepening of the storm. Zhang et al. (2002) investigate the significant influences of upper-level PVAs on a family of surface frontal cyclogenesis with the piecewise PV inversion. Using a modified PV inversion scheme of WZ03, Zhang and Kieu (2006) examine the quasi-balanced secondary circulations associated with diabatic heating, vertical wind shear, and the PBL friction using the PV–omega equations system.

The NLB is especially useful above the PBL where the gradient wind balance is valid for the rotational flows within an error of less than 10% (Zhang et al. 2001), and similarly for the PV-inverted rotational flows based on the NLB constraint (see WZ03). Shapiro and Möller (2003) use the asymmetric balance theory to examine the impact of asymmetrical flows on the intensification of Hurricane Opal (1995). As compared to the small divergence assumed in the NLB models, the asymmetric balance theory provides little restriction on the magnitude of divergence. However, WZ03's PV–omega equations system is shown to be capable of recovering almost all typical features in a hurricane, including intense convergence in the PBL, the sloping radius of maximum wind (RMW), a thermal inversion above the PBL in the eye, organized updrafts in the eyewall and subsidence in the eye, and upper-level anticyclonic-divergent outflows.

In essence, piecewise PV inversion is an algorithm that allows one to separate a total PVA within a volume into different patches (pieces) so that one can examine the balanced or quasi-balanced perturbation flows associated with each of the PV patches as well as their interactions, as detailed by DE91, Davis (1992), and Huo et al. (1999). A mathematical presentation of the piecewise PV inversion algorithm begins with the following nonlinear balance and PV equations:

$$\nabla^2 \Phi = \nabla_h (f \nabla_h \Psi) + 2J \left(\frac{\partial \Psi}{\partial x}, \frac{\partial \Psi}{\partial y} \right) \quad (1)$$

and

$$q = \frac{1}{r(z)G} \left[(f + \nabla_h^2 \Psi) \frac{\partial^2 \Phi}{\partial z^2} - \frac{\partial^2 \Psi}{\partial x \partial z} \frac{\partial^2 \Phi}{\partial x \partial z} - \frac{\partial^2 \Psi}{\partial y \partial z} \frac{\partial^2 \Phi}{\partial y \partial z} \right], \quad (2)$$

where q denotes PV, Φ and Ψ are the geopotential height and streamfunction, respectively, $z = [1 - (P/P_0)^{R/C_p}] (C_p \theta_0/g)$ is the vertical pseudoheight coordinate, G is the gravitational constant, $r(z) = \rho_0 (P/P_0)^{C_v/C_p}$ is pseudodensity, and θ_0 is the reference temperature at 1000 hPa. Since we are interested in the 3D circulations associated with the lower- to upper-level PVAs, the frictional effects of the PBL are ignored herein [i.e., in Eq. (1); see WZ03].

Obtaining the balanced flows associated with a PVA piece involves the following steps: a) obtain the 3D distribution of PV q , b) define the basic state or mean PV in 3D \bar{q} and then compute the corresponding balanced mass $\bar{\Phi}$ and winds $\bar{\Psi}$, c) subtract \bar{q} from the total q to obtain a total PVA q' , d) select a PVA piece q'_i of interest out of the total PVA q' , and finally e) perform a piecewise PV inversion to find the pertinent balanced perturbations Φ'_i and Ψ'_i associated with the q'_i in question.

An important requirement for piecewise PV inversion is to ensure the validity of the superposition principle: the summation of all balanced perturbations associated with all pieces must equal to the total balanced perturbation associated with the sum of all PV pieces; that is,

$$\Psi' = \sum_{i=1}^N \Psi'_i \quad \text{and} \quad \Phi' = \sum_{i=1}^N \Phi'_i \quad \text{if} \quad q' = \sum_{i=1}^N q'_i, \quad (3)$$

where Ψ' and Φ' are balanced flows associated with q' , Ψ'_i and Φ'_i are balanced flows associated with q'_i , and N is the number of PVA pieces. Note that PVAs do not have to be much smaller than the associated total PV as long as the resulting inverted nonlinear perturbation terms are small. Note also that arbitrary partitioning of the total PVA into different pieces may cause discontinuities at the edges of each piece, unless they are well localized and separable. These discontinuities may lead to the violation of the superposition principle, as discussed by Egger (2008), such that piecewise PV inversion would be no longer meaningful. It should be mentioned that there are many ways to partition the PVA into pieces to ensure the superposition principle. DE91's methodology appears to be one of the most practical ways to perform piecewise PV inversion, and it is recapitulated as follows:

$$\nabla^2 \Phi'_i = \nabla (f \nabla \Psi'_i) + 2 \left(\frac{\partial^2 \Psi^*}{\partial x^2} \frac{\partial^2 \Psi'_i}{\partial y^2} - 2 \frac{\partial^2 \Psi^*}{\partial x \partial y} \frac{\partial^2 \Psi'_i}{\partial x \partial y} + \frac{\partial^2 \Psi^*}{\partial y^2} \frac{\partial^2 \Psi'_i}{\partial x^2} \right) \quad \text{and} \quad (4)$$

$$q'_i = (f + \nabla^2 \Psi^*) \frac{\partial^2 \Phi'_i}{\partial z^2} + \nabla^2 \Psi'_i \frac{\partial^2 \Phi^*}{\partial z^2} - \left(\frac{\partial^2 \Psi^*}{\partial x \partial z} \frac{\partial^2 \Phi'_i}{\partial x \partial z} - \frac{\partial^2 \Phi^*}{\partial x \partial z} \frac{\partial^2 \Psi'_i}{\partial x \partial z} \right) - \left(\frac{\partial^2 \Psi^*}{\partial y \partial z} \frac{\partial^2 \Phi'_i}{\partial y \partial z} - \frac{\partial^2 \Phi^*}{\partial y \partial z} \frac{\partial^2 \Psi'_i}{\partial y \partial z} \right), \quad (5)$$

where $(\Phi, \Psi)^* = (\bar{\Phi}, \bar{\Psi}) + \frac{1}{2} \sum_{i=1}^N (\Phi'_i, \Psi'_i)$ and $q' = \sum_{i=1}^N q'_i$.

The above approach, however, still contains some arbitrariness in computing the mean states. One may follow DE91's procedures by computing a 3D temporal (or spatial) \bar{q} and then performing the piecewise PV inversion of Eqs. (4) and (5) to obtain the mean balanced mass and wind perturbation fields. In a different way than applied to hurricanes, WZ03 seek the balanced mean state by first taking the azimuthal average of $\bar{\Phi}$. Equation (1) is then inverted to give $\bar{\Psi}$, and finally \bar{q} is calculated from Eq. (2). Similarly, one may calculate $\bar{\Psi}$ first, and then $\bar{\Phi}$ and \bar{q} . In this way, \bar{q} is automatically balanced with $\bar{\Psi}$ and $\bar{\Phi}$ without inverting the mean PV. Apparently, the balanced mean states may be obtained differently, depending on the convenience of piecewise PV inversion or the scientific problems to be addressed.

Although piecewise PV inversion appears to be applicable even for high Rossby number flows (Davis 1992),

WZ03 note that the elliptic condition for Eq. (4) may not be always satisfied when it is applied to hurricane vortices because of the presence of large anticyclonic shear often occurring outside the RMW. This problem could also appear in extratropical cyclones, and it can be circumvented by assuming that PV is larger than a positive threshold value (see DE91). To minimize the distortion of balanced flows, WZ03 introduce a free parameter ε into Eqs. (4) and (5) and cast these equations into a new form such that the elliptic condition could be modified as follows:

$$\left(\varepsilon f + 2\varepsilon \frac{\partial^2 \bar{\Psi}}{\partial x^2} + \frac{\partial^2 \bar{\Phi}}{\partial z^2} \right) \left(\varepsilon f + 2\varepsilon \frac{\partial^2 \bar{\Psi}}{\partial y^2} + \frac{\partial^2 \bar{\Phi}}{\partial z^2} \right) - 4\varepsilon^2 \left(\frac{\partial^2 \bar{\Psi}}{\partial x \partial y} \right)^2 > 0. \quad (6)$$

Evidently, Eq. (6) can be satisfied as long as ε is between 0 and 1, thereby making the piecewise PV inversion more flexible. Note that WZ03's inversion algorithm is only suitable for one PVA piece, so our purpose here is to extend this one-piece PV inversion to multiple PVA pieces. We start from the following equations system, following WZ03:

$$\begin{aligned} \left(\varepsilon f + \frac{\partial^2 \bar{\Phi}}{\partial z^2} \right) \nabla^2 \Psi'_i = q'_i - (f + \nabla^2 \bar{\Psi}) \frac{\partial^2 \Phi'_i}{\partial z^2} + \frac{\partial^2 \bar{\Psi}}{\partial x \partial z} \frac{\partial^2 \Phi'_i}{\partial x \partial z} + \frac{\partial^2 \bar{\Phi}}{\partial x \partial z} \frac{\partial^2 \Psi'_i}{\partial x \partial z} + \frac{\partial^2 \bar{\Psi}}{\partial y \partial z} \frac{\partial^2 \Phi'_i}{\partial y \partial z} + \frac{\partial^2 \bar{\Phi}}{\partial y \partial z} \frac{\partial^2 \Psi'_i}{\partial y \partial z} \\ - \frac{1}{2} \left(\sum_{n=1}^N \nabla^2 \Psi'_n \frac{\partial^2 \Phi'_i}{\partial z^2} + \nabla^2 \Psi'_i \sum_{n=1}^N \frac{\partial^2 \Phi'_n}{\partial z^2} \right) + \frac{1}{2} \left(\sum_{n=1}^N \frac{\partial^2 \Psi'_n}{\partial x \partial z} \frac{\partial^2 \Phi'_i}{\partial x \partial z} + \sum_{n=1}^N \frac{\partial^2 \Phi'_n}{\partial x \partial z} \frac{\partial^2 \Psi'_i}{\partial x \partial z} \right) \\ + \frac{1}{2} \left(\sum_{n=1}^N \frac{\partial^2 \Psi'_n}{\partial y \partial z} \frac{\partial^2 \Phi'_i}{\partial y \partial z} + \sum_{n=1}^N \frac{\partial^2 \Phi'_n}{\partial y \partial z} \frac{\partial^2 \Psi'_i}{\partial y \partial z} \right) + \varepsilon \left[\nabla^2 \Phi'_i - \beta \frac{\partial \Psi'_i}{\partial y} - 2 \left(\frac{\partial^2 \bar{\Psi}}{\partial x^2} \frac{\partial^2 \Psi'_i}{\partial y^2} - 2 \frac{\partial^2 \bar{\Psi}}{\partial x \partial y} \frac{\partial^2 \Psi'_i}{\partial x \partial y} \right. \right. \\ \left. \left. + \frac{\partial^2 \bar{\Psi}}{\partial y^2} \frac{\partial^2 \Psi'_i}{\partial x^2} \right) - \left(\sum_{n=1}^N \frac{\partial^2 \Psi'_n}{\partial x^2} \frac{\partial^2 \Psi'_i}{\partial y^2} - 2 \sum_{n=1}^N \frac{\partial^2 \Psi'_n}{\partial x \partial y} \frac{\partial^2 \Psi'_i}{\partial x \partial y} + \sum_{n=1}^N \frac{\partial^2 \Psi'_n}{\partial y^2} \frac{\partial^2 \Psi'_i}{\partial x^2} \right) \right] \quad \text{and} \quad (7) \end{aligned}$$

$$\begin{aligned} \nabla^2 \Phi'_i + (f + \nabla^2 \bar{\Psi}) \frac{\partial^2 \Phi'_i}{\partial z^2} = q'_i - \nabla^2 \Psi'_i \frac{\partial^2 \bar{\Phi}}{\partial z^2} + f \nabla^2 \Psi'_i + \beta \frac{\partial \Psi'_i}{\partial y} + \frac{\partial f_x}{\partial x} + \frac{\partial f_y}{\partial y} \\ - \frac{1}{2} \left(\sum_{n=1}^N \nabla^2 \Psi'_n \frac{\partial^2 \Phi'_i}{\partial z^2} + \nabla^2 \Psi'_i \sum_{n=1}^N \frac{\partial^2 \Phi'_n}{\partial z^2} \right) + \frac{\partial^2 \bar{\Psi}}{\partial x \partial z} \frac{\partial^2 \Phi'_i}{\partial x \partial z} + \frac{\partial^2 \bar{\Phi}}{\partial x \partial z} \frac{\partial^2 \Psi'_i}{\partial x \partial z} + \frac{\partial^2 \bar{\Psi}}{\partial y \partial z} \frac{\partial^2 \Phi'_i}{\partial y \partial z} \\ + \frac{\partial^2 \bar{\Phi}}{\partial y \partial z} \frac{\partial^2 \Psi'_i}{\partial y \partial z} + \frac{1}{2} \left(\sum_{n=1}^N \frac{\partial^2 \Psi'_n}{\partial x \partial z} \frac{\partial^2 \Phi'_i}{\partial x \partial z} + \sum_{n=1}^N \frac{\partial^2 \Phi'_n}{\partial x \partial z} \frac{\partial^2 \Psi'_i}{\partial x \partial z} \right) + \frac{1}{2} \left(\sum_{n=1}^N \frac{\partial^2 \Psi'_n}{\partial y \partial z} \frac{\partial^2 \Phi'_i}{\partial y \partial z} + \sum_{n=1}^N \frac{\partial^2 \Phi'_n}{\partial y \partial z} \frac{\partial^2 \Psi'_i}{\partial y \partial z} \right) \\ + 2 \left(\frac{\partial^2 \bar{\Psi}}{\partial x^2} \frac{\partial^2 \Psi'_i}{\partial y^2} - 2 \frac{\partial^2 \bar{\Psi}}{\partial x \partial y} \frac{\partial^2 \Psi'_i}{\partial x \partial y} + \frac{\partial^2 \bar{\Psi}}{\partial y^2} \frac{\partial^2 \Psi'_i}{\partial x^2} \right) \\ + 2 \left(\frac{1}{2} \sum_{n=1}^N \frac{\partial^2 \Psi'_n}{\partial x^2} \frac{\partial^2 \Psi'_i}{\partial y^2} - 2 \frac{1}{2} \sum_{n=1}^N \frac{\partial^2 \Psi'_n}{\partial x \partial y} \frac{\partial^2 \Psi'_i}{\partial x \partial y} + \frac{1}{2} \sum_{n=1}^N \frac{\partial^2 \Psi'_n}{\partial y^2} \frac{\partial^2 \Psi'_i}{\partial x^2} \right), \quad (8) \end{aligned}$$

in which Eq. (7) is obtained by multiplying Eq. (4) by ε and adding it into Eq. (5), and similarly by subtracting to obtain Eq. (8). To some extent, the introduction of the ε parameter can be considered as performing iterations of underrelaxation, which is sometime necessary to ensure the convergence of elliptic equations. Our experiments with multiple PVAs indicate that the iterations of Eqs. (7) and (8) converge when ε is taken between 0.1 and 0.18.

Since the PV inversion only deals with the balanced dynamics of rotational flows, the PV–omega system developed by WZ03 can be employed to examine the secondary (or transverse) circulations as a quasi-balanced response to a diabatic heating profile. This PV–omega system consists of an ω equation in the vertical upward-pointing, z coordinates (Hoskins and Bretherton 1972), the vorticity equation, and the continuity equation (see WZ03). Given balanced flows associated with a PVA, the PV–omega system will provide the 3D distribution of secondary circulations that are induced by the dry dynamical, latent heating, or frictional processes. More detailed description of the PV–omega system can be found in WZ03 and Zhang and Kieu (2006).

3. Piecewise PV inversion algorithm

Unlike the inversion of one PVA piece (i.e., $N = 1$), it is no longer possible to obtain Ψ'_i and Φ'_i by inverting Eqs. (7) and (8), given *only* q'_i for the case of N PVA pieces. This is because Eqs. (7) and (8) now contain $2N$ variables: N unknown wind fields Ψ'_i ($i = 1, \dots, N$) and N unknown mass fields Φ'_i ($i = 1, \dots, N$), and they compose a system of $2N$ nonlinear equations for N PVA pieces that need to be solved simultaneously. The convergence of iterating the $2N$ nonlinear equations is sensitive to various model parameters, the first guess, and boundary conditions if one employs a simple iterative method.

In DE91's algorithm, such iteration of the $2N$ equations is bypassed by first inverting the total and the mean PV. By subtracting the balanced mean from the total fields, the total perturbations (i.e., $\sum_{i=1}^N \Psi'_i$ and $\sum_{i=1}^N \Phi'_i$) can be obtained directly and therefore the system of Eqs. (7) and (8) is now closed. Of course, this approach requires an inversion of not only the system of Eqs. (7) and (8) but also the total PV [i.e., Eqs. (1) and (2)], for which the nonlinearity often poses some challenge for convergence. In the linear framework, we propose an alternative approach that does not require a separate inversion of the total PV. This is desirable for a system in which perturbations are much smaller than the mean such that nonlinearity is negligible.

To demonstrate the above idea, suppose that N PVA pieces q'_i ($i = 1, 2, \dots, N$) with appropriate boundary

conditions are known in advance, and we wish to find the 3D balanced perturbations Φ'_k and Ψ'_k associated with each of the PVA pieces. Our piecewise PV inversion algorithm consists of the following steps: (i) sum up all PVA pieces q'_i to obtain a total PVA piece q' , and similarly for all the boundary conditions associated with each PVA piece; (ii) solve Eqs. (7) and (8) for this total q' in the same way as described by WZ03 to yield Ψ' and Φ' associated with the total PVA q' (because there is only one PVA piece, iterations will converge easily); (iii) replace the summations of Ψ'_i and Φ'_i in Eqs. (7) and (8) by Ψ' and Φ' , which are obtained in the second step above (e.g., $\sum_{n=1}^N (\partial^2 \Psi'_n / \partial x \partial y)$ by $\partial^2 \Psi' / \partial x \partial y$, $\sum_{n=1}^N (\partial^2 \Psi'_n / \partial x \partial z)$ by $\partial^2 \Psi' / \partial x \partial z$, etc.; clearly this complies with the superposition principle); and (iv) perform inversions of each piece q'_k to find the corresponding balanced perturbation Ψ'_k and Φ'_k as needed. In this last step, the inversion will involve only two equations for the two unknowns, Ψ'_k and Φ'_k , given the PVA piece q'_k and its appropriate boundary conditions. It is no longer necessary to know all the other Ψ'_j and Φ'_j ($j \neq k$) simultaneously when solving for the piece q'_k since they are already included in Ψ' and Φ' obtained in step 2. With this approach, the inversion is much easier to carry out than the simultaneous iterations of $2N$ equations or the inversion of the total PV. Note that unless the boundary conditions for all PVA pieces are homogeneous, attention must be paid to the boundary conditions of each piece to ensure the validity of the superposition principle.

4. Hurricane inner-core PV anomalies

In this section, we first use the piecewise PV inversion algorithm described in the preceding section to examine the impact of different types of PVAs on the hurricane intensity and structures. As mentioned earlier and shown in Fig. 1, PVAs in a hurricane may include a PVA core above the PBL in the eye, PVA rings associated with the inner or outer eyewalls, and an upper-level PVA core. Although this partitioning is based on the vertical distribution of the total PV (e.g., in Fig. 1), it is also held for PVAs after defining the mean state as an azimuthal average. For the purpose of this study, we will focus on the above-mentioned PVAs because it is these PVAs that, once generated, could propagate within hurricanes and induce some structural and intensity changes. Unlike the balanced mean vortex, these PVAs may not be in the gradient wind balance. But the piecewise PV inversion will filter out any unbalanced flow, rendering the final total flows dynamically balanced. Presumably, the impact of this modified flow on hurricane intensity is small.

a. Experimental design

To make our study as general as possible, we will perform piecewise PV inversion with idealized PVAs to characterize the abovementioned features. A balanced mean hurricane vortex (see Fig. 2a) is given a priori, following WZ03, by use of an 86-h cloud-resolving simulation of Hurricane Bonnie (1998), at which time it becomes more axisymmetric and reaches its mature stage (see Zhu et al. 2004). Note that the choice of Bonnie as a mean vortex is to create an idealized vortex with a realistic hurricane-like structure. Part of the reason to select this simulated storm is its apparent configuration of double eyewalls, which will be examined in the next section. Bonnie's mean vortex has typical peak PV of greater than 30 PVU at $z = 3$ and 6 km in the eye and peak tangential winds of more than 45 m s^{-1} in the eyewall. Because of the exclusion of frictional effects in Eq. (1), the peak winds occur at the surface.

Three PVAs of the following forms are superimposed on the mean vortex:

$$q_e = A_1 \sin\left(\frac{\pi z}{H_e}\right) \exp\left[-\left(\frac{z}{H_e}\right)^{\alpha_e}\right] \exp\left[-\left(\frac{r-r_c}{R_e}\right)^2\right], \quad (9a)$$

$$q_b = A_1 \exp\left[-\left(\frac{z-z_b}{H_b}\right)^{\alpha_b}\right] \exp\left[-\left(\frac{r}{R_b}\right)^2\right], \quad (9b)$$

$$q_u = A_1 \exp\left[-\left(\frac{z-z_u}{H_u}\right)^{\alpha_u}\right] \exp\left[-\left(\frac{r}{R_u}\right)^2\right], \quad (9c)$$

where A_1 denotes the amplitude of each PVA; H and R represent the vertical and horizontal scales of q , respectively; and the subscripts e , b , and u indicate the eyewall and the lower and upper levels, respectively. See Table 1 for the dimensions and magnitudes of all parameters. Because the PVAs given by Eq. (9) decrease rapidly to zero in both radial and vertical directions, homogeneous boundary conditions for all the PV pieces are assumed (Egger 2008). By assuming explicitly the PVA forms of Eq. (9), the discontinuity problem that may arise when partitioning PVA pieces is also eliminated.

A control case (CTL) is designed in which the maximum magnitudes of all the superimposed PVAs (i.e., A_1) are set to 10 PVU. Following the algorithm proposed in section 3, we first sum up all PVA pieces given by Eq. (9) and perform an inversion for the summed PVA to obtain the total balanced perturbations. Using the total balanced perturbations, the perturbation associated with each piece is then obtained by inverting each piece individually.

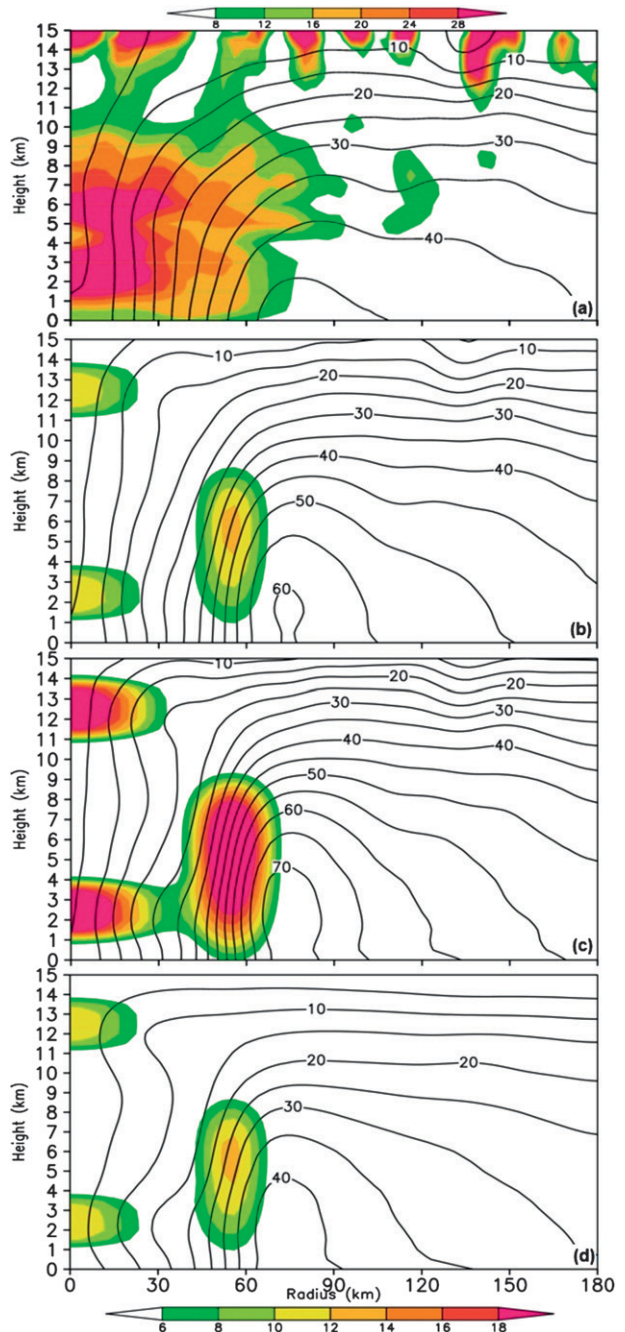


FIG. 2. R - z cross sections of tangential winds, at intervals of 5 m s^{-1} , for (a) the mean hurricane vortex, (b) the control case (CTL), (c) the doubled PVA experiment (DPV), and (d) the halved mean-vortex intensity experiment (HVX). Shadings denote PV in (a) but PVAs in (b)–(d). Note that PVAs have a peak value of 10 PVU in (b) and (d) but 20 PVU in (c). The mean vortex is taken from an 89-h cloud-resolving simulation of Hurricane Bonnie (1998); see Zhu et al. (2004).

TABLE 1. List of the parameters used in Eqs. (9) and (11).

Parameter	Remark	Value
A_1	Amplitude of each PVA	10 or 20 PVU
H_e	Vertical scale of the PVA for the eyewall piece	12×10^3 m
R_e	Horizontal radius of the PVA for the eyewall piece	15×10^3 m
α_e	Decreasing rate of the PVA for the eyewall piece	4
H_b	Same as H_e but for the lower-level PVA piece	12×10^3 m
R_b	Same as R_e but for the lower-level PVA piece	15×10^3 m
α_b	Same as α_e but for the lower-level PVA piece	4
H_u	Same as H_e but for the upper-level PVA piece	12×10^3 m
R_u	Same as R_e but for the upper-level PVA piece	15×10^3 m
α_u	Same as α_e but for the upper-level PVA piece	4
r_c	Central radius of the inner eyewall	55×10^3 m
r_o	Central radius of the outer eyewall	120×10^3 m
Q_o	Diabatic heating rates in the outer eyewall	30 K h^{-1}
Q_i	Diabatic heating rates in the inner eyewall	30 K h^{-1}

Two sensitivity experiments are conducted by either (a) doubling the amplitudes of the three PVAs (DPV experiment; i.e., $A_1 = 20$ PVU) or (b) halving the tangential winds of the mean vortex (HVX experiment) but with the same PVA amplitude A_1 as that in the CTL experiment. Note that HVX could be alternatively obtained by reducing the total PV of the mean vortex by half and then inverting it to yield $\bar{\Phi}$ and $\bar{\Psi}$.

Figures 2b–d show the vertical cross sections of the PVAs given by Eqs. (9a)–(9c) and their corresponding total balanced flows (i.e., $\mathbf{V} = |\mathbf{V} \times \Psi|$, where $\Psi = \bar{\Psi} + \Psi'_u + \Psi'_b + \Psi'_e$) for the CTL, DPV, and HVX experiments, respectively. One can see that the PVA structures share many similarities to those shown in Fig. 1, including the eyewall, upper-core, and lower-core PVAs, except that the eyewall PVA q_e does not tilt with height; the eyewall tilt will be considered in the next section in association with double eyewalls. The total balanced flows, which are the sum of the background rotation and the balanced perturbation flows, show significant variations in these experiments with the peak tangential winds varying between 40 and 70 m s^{-1} , depending on the strength of the background vortex or PVA magnitudes. It should be mentioned that halving the mean tangential flows does not decrease the mean PV by the same factor. This is because the reduction of tangential flows (and equally for the vertical shears) will reduce radial gradients

in the mean potential temperature under the thermal wind constraint, and the static stability in the eye.

b. The control case

Figures 3a–c show the tangential perturbation flows associated with the three PVAs (q_u , q_e , and q_b) given by Eq. (9) for the CTL case. As can be expected, all the PVA pieces induce significant cyclonic flows around their centers. The induced maximum tangential wind is more than 14 m s^{-1} for the eyewall PVA q_e (Fig. 3b), while the q_b - and q_u -induced perturbation winds are slightly over 5 and 4 m s^{-1} , respectively. The smaller contributions of q_b and q_u than those of the q_e are due mostly to their shallow depths and smaller volumes. Of importance is that, unlike the previous studies of baroclinic vortices (e.g., Huo et al. 1998), there is little evidence of the vertical interaction between the upper- and lower-level PVAs in the eye within the hurricane environment. Instead, both q_b and q_u tend to enhance the q_e -induced cyclonic rotation, especially inside the RMW. As a result, the tangential flows associated with q_b and q_u tend to shift the RMW inward (Figs. 3a,c) while the q_e -induced flows tend to enhance (reduce) the background vortex outside (inside) the eyewall with a much larger magnitude outside than inside.

It is of interest to note that even though q_b and q_u are embedded in the background flows of different strengths, their balanced responses are only slightly different in magnitude (see Figs. 3a,c). To examine the absolute impact of the PVAs, we hereafter define either the depth or radius of their balanced influence with a speed threshold of 2 m s^{-1} . Such a threshold rather than a relative ratio is chosen because it is this absolute measure that could indicate notable hurricane intensity change. Of course, one can choose any threshold value, and the speed of 2 m s^{-1} is adopted herein because its isotach is always inside the inversion domain. One can see that the perturbation flows associated with q_u and q_b have similar influence radii (i.e., 60–90 km), whereas the influence radius for q_e is 120–150 km in the low to midtroposphere but several hundreds of kilometers in the upper outflow layer. Details about this scaling behavior will be examined further in relation to the sensitivity experiments presented in the next subsection.

Figures 3d–f show the corresponding responses of the perturbation pressure and the induced potential temperature perturbation θ' to the three different PVAs. In agreement with the balanced cyclonic flows, all the PVAs induce a low pressure system that peaks at the bottom of their volumes with a warm core above a cold dome. Such a vertical distribution of the PVA-induced warmth and coldness changes the local static stability in their influencing layers (cf. Figs. 3a–c and 3d–f), while their horizontal

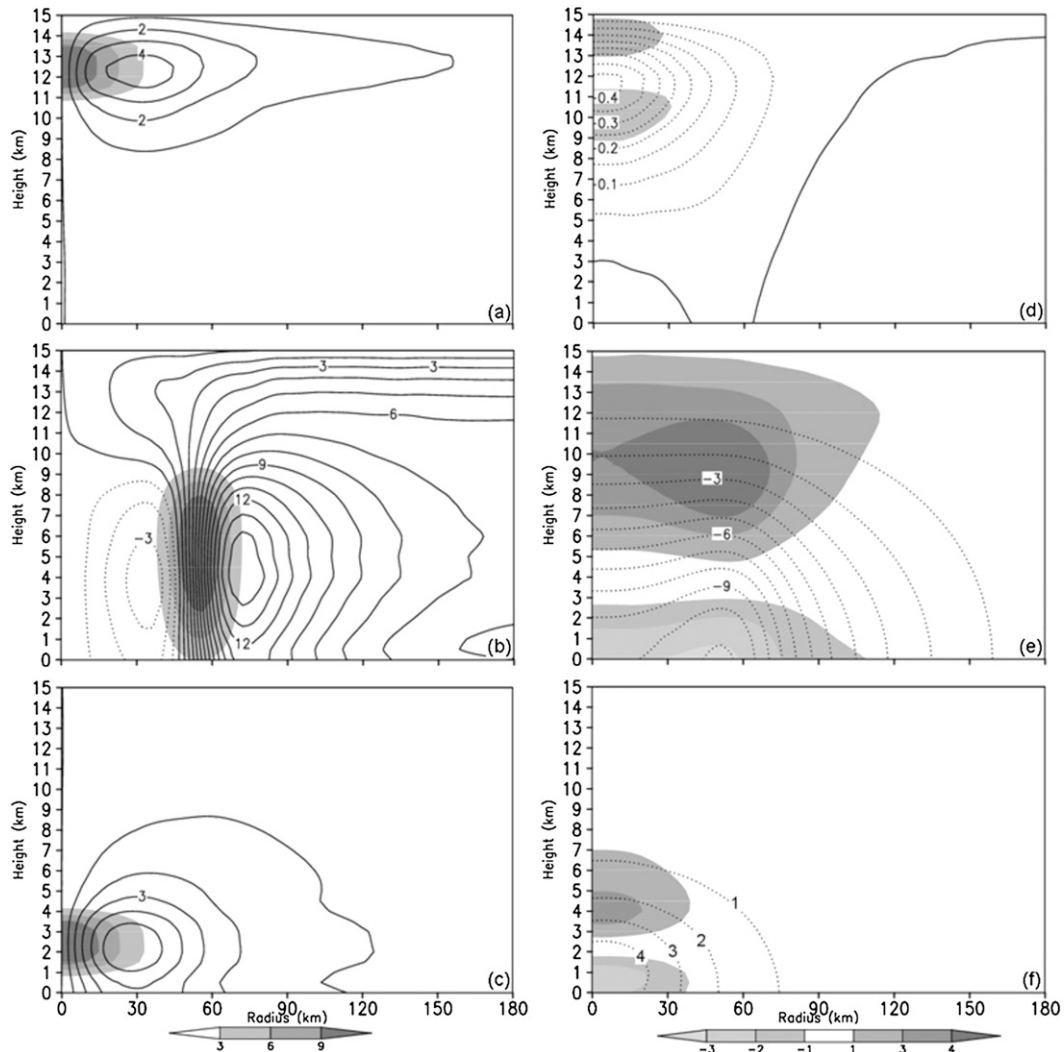


FIG. 3. R - z cross sections associated with (top) q_u , (middle) q_e , and (bottom) q_b for (a)–(c) the perturbation tangential winds contoured at intervals of 1 m s^{-1} and the corresponding PV piece shaded at intervals of 3 PVU and (d)–(f) the perturbation pressure (contoured at intervals of 1 hPa for q_e and q_b , and at intervals of 0.05 hPa for q_u) and the potential temperature perturbations (shaded, $^{\circ}\text{C}$).

gradients comply with the thermal wind relation, generating positive (negative) vertical wind shear outside in the induced cold (warm) layer.

Like the perturbation flows, the most significant pressure response in terms of the magnitude of the induced perturbation and penetration depth is from q_e , followed by q_b , with the minimum central pressure deficit of 11 and 5 hPa, respectively. Although the usually observed warm core in the eye and the minimum central pressure could still be attributed mostly to the balanced constraint by the mean vortex, Fig. 3e shows that the balanced potential temperature perturbation induced by the eyewall PVA appears to contribute also to the enhancement of the warm core. Such balanced contribution is

hydrostatically related to the low pressure anomalies induced by q_e at the center. Note, however, that q_b tends to contribute more effectively than the other two PVAs to the minimum central pressure if the same magnitude of the mass-weighted PVA is superimposed. This indicates that the hurricane intensity fluctuations could be closely connected to any processes leading to an aggregation of PVAs in an inversion layer above the PBL in the eye (see Fig. 1).

c. Sensitivity experiments

After examining the impact of different types of PVAs, it is desirable to see how sensitive the dynamical responses are to different intensities of the PVAs and the

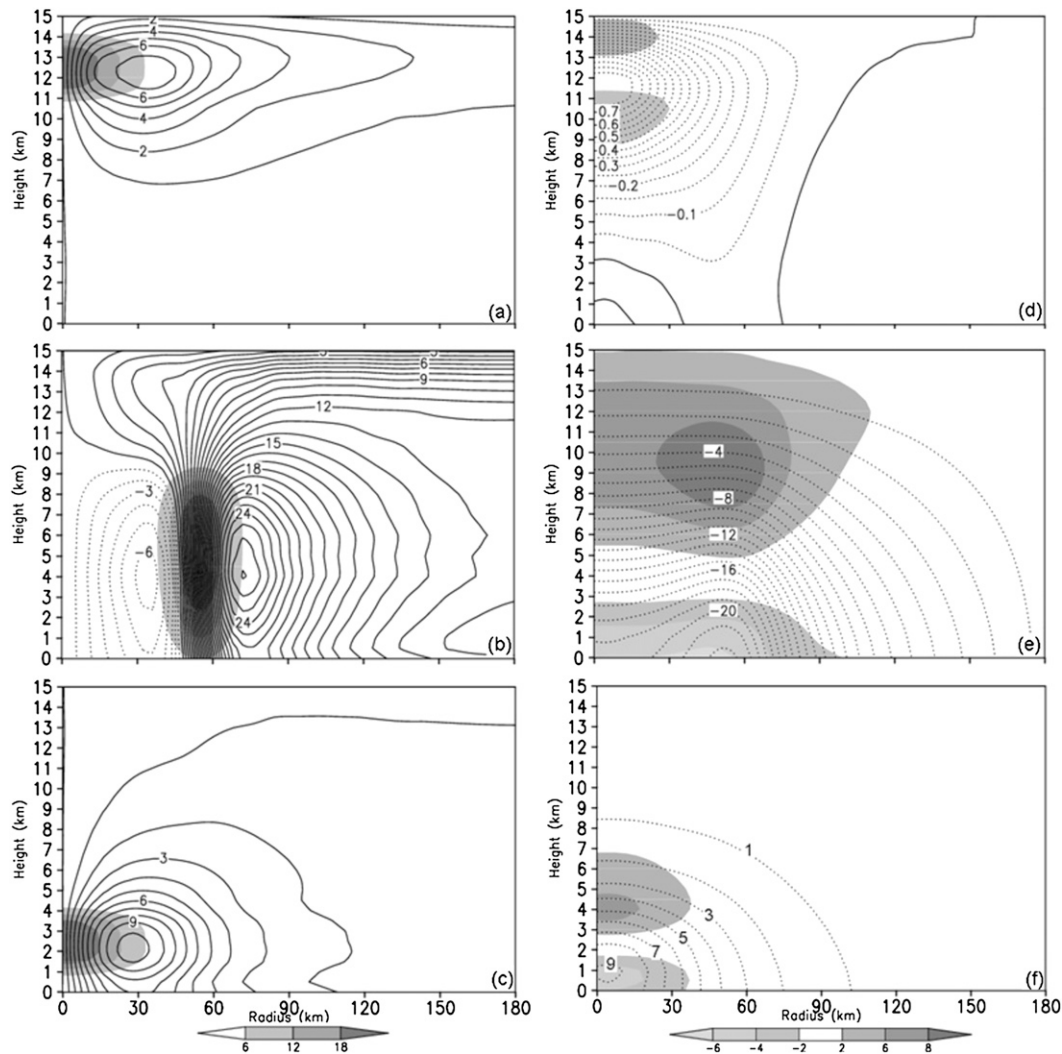


FIG. 4. As in Fig. 3, but for the doubled PV anomaly experiment (DPV). Also note that the shading scales are doubled.

background vortex. Similar issues have been discussed in part in the early work of HRM in terms of the penetration depth H of balanced responses, but only for synoptic-scale flows. HRM's concept of the penetration depth requires that the horizontal influence scale L of a perturbation flow associated a given PVA is known a priori. However, unless some relationship between L of a PVA and the influence scale R of its related perturbation flows can be provided, the latter is generally unknown a priori for a given PVA. It should be mentioned that for a strict linear PVA inversion the scale of the balanced response will be the same as the scale of PVAs (i.e., $R = L$). Nevertheless, HRM's scale analysis is still applicable for the piecewise inversion using Eqs. (7) and (8) because the scales of the balanced influences depend not only on the scales of the PVA pieces but also

on the strength of the background vortex that appears in the coefficients of the elliptic operator. In this subsection, we will not assume a horizontal influence scale a priori but attempt to understand the variations of both the horizontal and vertical scales of perturbation flows under different background flows and PVA intensities.

Figure 4 shows the radius–height cross sections of the PVA-induced perturbation flows in the DPV experiment. Obviously, doubling the PVA intensities nearly doubles their associated balanced responses. For example, the peak tangential perturbation winds induced by q_w , q_e , and q_b exceed 7, 27, and 10 m s^{-1} compared to 4, 14, and 5 m s^{-1} in CTL, respectively (cf. Figs. 4a–c and 3a,c). Similarly, the PVA-induced temperature and pressure perturbations are nearly double those in CTL (cf. Figs. 4d–f and 3d–f). Such near-linear behaviors are

attributable to the fact that the most weighted forcing term is associated with the PVAs [i.e., the first term on the rhs of Eqs. (7) and (8), as also demonstrated by Davis (1992)].

Of importance is that doubling the PVAs intensities also results in significant increases of not only the depth H but also the radius R of the influence by nearly the same factor (about 60%–70%; see Fig. 4). Because the horizontal scale could not be easily given in advance, a better measurement for the sensitivity of the balanced response is the ratio of H/R , which can be put into the following form:

$$\frac{H}{R} = \frac{1}{N^2} \sqrt{\frac{\Omega q' \rho_o G}{\theta_0}}. \quad (10)$$

While Eq. (10) is derived from the aspect ratio of the elliptic PV operator (see HRM), it can be expected to be a reasonable measurement for the relative scales of the absolute influence of the perturbations as we are working with the ratio rather than the actual scales. It appears from Eq. (10) that the ratio H/R should increase proportionally to the square root of q' (i.e., by a factor of $\sqrt{2}$) as a PVA is doubled in intensity. A comparison between Figs. 3 and 4 shows that this ratio is nonetheless roughly the same (i.e., $H/R \approx 0.08$ in both DPV and CTL). This can only be explained if we also include changes in the local static stability N^2 as discussed earlier. Indeed, N^2 increases from $5 \times 10^{-5} \text{ s}^{-2}$ in CTL to about 10^{-4} s^{-2} in DPV below the PVA cores, as can be estimated from Figs. 3 and 4. The changes in the static stability are sufficient to offset the doubled intensities of the PVAs, thereby causing little changes in the ratio H/R . Apparently, the altered static stability has played a significant role in determining the scales of the balanced responses, but its impact has been previously ignored when applying HRM's penetration depth concept to PVAs associated with extratropical cyclones or MCSs. Note that the changes of the ratio H/R will be more complete if we also take into account the changes of the absolute angular velocity Ω as the PVAs are doubled. However, the small magnitude of the perturbation flows compared to that of the background vortex results in only a small percentage increase of Ω , and so does the ratio H/R , in this DPV experiment.

Doubling the PVAs from 10 to 20 PVU also roughly doubles θ' and the pressure perturbation (e.g., from 2°, 5°, and 3.5°C to 4°, 8°, and 5°C, and from 0.4, 11, and 5 hPa to 1, 22, and 10 hPa, associated with q_u , q_e , and q_b , respectively; cf. Figs. 4d–f and 3d–f). Like the perturbation flows, the penetration depth and horizontal influence radius of the pressure perturbations increase

significantly as the PVAs are doubled in intensity. We can see from Fig. 4 that the q_u - and q_b -induced flows now begin to show some weak vertical interactions in the eye, while remaining their individual strong interactions with the q_e -induced flows. Nevertheless, the upper PVA q_u always has little direct influence on the surface development even with its intensity doubled, as seen in the CTL and DPV experiments, and it is the lower-level PVAs in the eyewall and eye that account more for hurricane intensity fluctuations.

When the basic-state vortex intensity is halved (HVX), the PVA-induced cyclonic flows are all enhanced, roughly by 25%–30%, except for the cyclonic return flow in the eye associated with q_e , which shows some notable weakening (Figs. 5a–c). The most significant enhancement occurs with q_e in the tangential flows outside the RMW, from 14 to 18 m s^{-1} . Again, such resilience of the perturbation flows to the background vortex, as also shown in CTL, could be attributed to the most weighted forcing PVAs on the rhs of Eqs. (7) and (8). Any change to the mean vortex intensity will cause most changes in the linear forcing terms [that is, the terms on the rhs of Eqs. (7) and (8) that contain products of the mean and perturbations, such as $(\partial^2 \Psi / \partial x \partial z)(\partial^2 \Phi' / \partial x \partial z)$]; they tend to produce smaller impacts on perturbation flows than those of the PVA-induced flows because of the smoothness of the mean variables.

In contrast, the horizontal influence radius of the PVA-induced perturbation flows shows significant expansions, from 40 km in CTL to 75 km in HVX, whereas the penetration depth is more or less the same between the two experiments. This causes the ratio H/R to decrease about 30%–40%, which is in agreement with Eq. (10b), considering that Ω (or the inertial stability) is nearly halved in HVX. Unlike in DPV, halving the mean vortex intensity only produces slight intensity changes in the mass field (cf. Figs. 5d–f and 3d–f). Thus, the reduction of Ω could lead to a decrease of H/R by a factor of $\sqrt{2}$ from the CTL case. This result appears to suggest that stronger hurricane vortices tend to localize the dynamical responses of PVAs horizontally but increase somewhat their penetration depths, as described by Eq. (10b). This large variation in the horizontal influence scale, as compared to the penetration depth, is a consequence of the reduction of the inertial stability in HVX.

Figure 6 shows how different intensities of the PVAs and the background vortex may influence the quasi-balanced secondary circulation. The latter is obtained by using WZ03's PV–omega inversion scheme with a peak heating rate $Q_{\max} = 30 \text{ K h}^{-1}$ collocated with the PVA center in the eyewall, based on Bonnie's heating profile. The CTL case exhibits an organized upward motion of

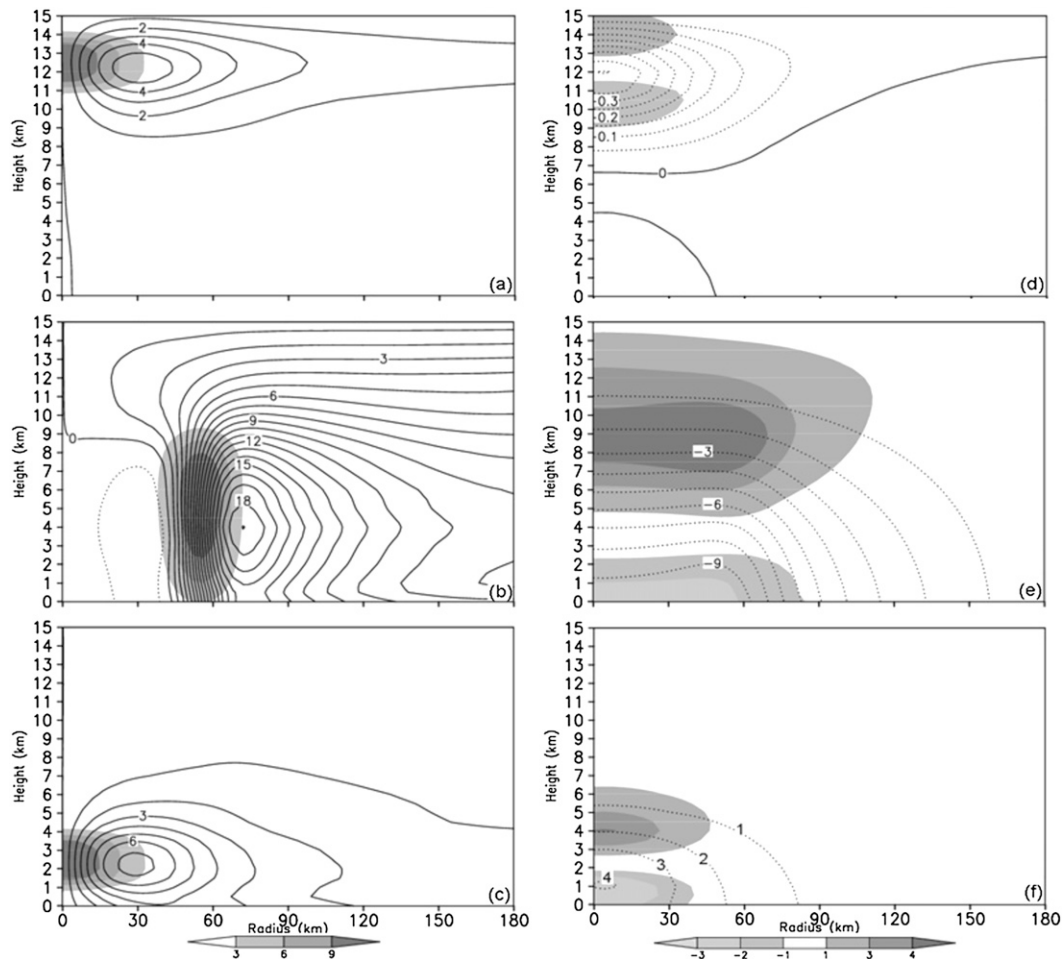


FIG. 5. As in Fig. 3, but for the halved mean-vortex intensity experiment (HVX).

more than 1.5 m s^{-1} in the eyewall with radial inflows and outflows in the lower and upper half of the troposphere, respectively, and subsidence in the eye (Fig. 6a), which are consistent with those shown in Zhang and Kieu (2006). Of importance is that doubling the PVAs produces a weaker secondary circulation (Fig. 6b), whereas the opposite occurs when the background vortex intensity is halved (Fig. 6c). The altered intensities in the secondary circulation could be understood in terms of the changes in static stability that provides resistance to vertical displacements, and the changes in inertial stability that provides resistance to radial displacements, as described by Eliassen's (1952) equation (see Hack and Schubert 1986). That is, the stronger the static stability (the inertial stability) induced by q_e , the weaker upward (radial) motion is in the eyewall (lower troposphere). It is apparent from the above discussions that doubling the PVA in the eyewall increases both the inertial stability and the static stability due to the enhanced cyclonic flows (cf. Figs. 2b,c) and thermal perturbations

(cf. Figs. 3e and 4e), respectively. The opposite is true with the mean vortex intensity halved (cf. Figs. 2b,d, 3e, and 5e). This implies again that stronger hurricanes will be more resilient to the influences of PVAs in the eyewall.

5. Eyewall replacement dynamics

Because of the important roles of double eyewalls in hurricane intensity changes, we wish to understand how the development of an outer eyewall would affect the hurricane inner-core dynamics during the eyewall replacement period in the balanced framework. Like in the CTL case, we define a mean vortex using an 89-h cloud-resolving simulation of Hurricane Bonnie (1998) at which time a double eyewall pattern is most evident (see Zhu et al. 2004). As mentioned before, we may treat the outer and inner eyewalls as two idealized rings of PVAs, referred to as q_o and q_i , respectively. They are given by the following forms:

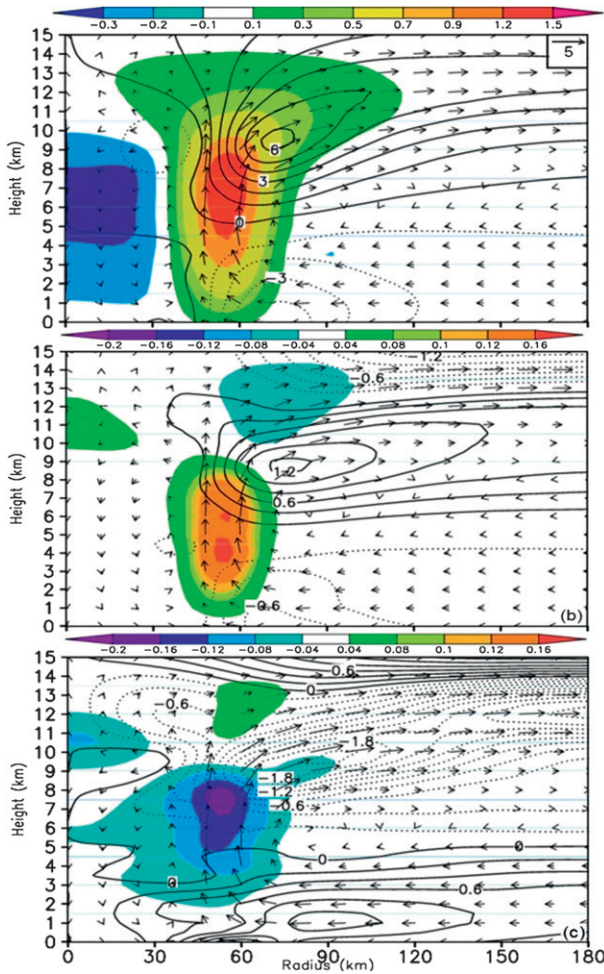


FIG. 6. R - z cross sections of (a) the quasi-balanced vertical motion (shaded, m s^{-1}) and the radial flows (contoured at intervals of 1 m s^{-1}) for the CTL case, (b) the differenced (CTL - DPV) vertical motion (shaded, m s^{-1}) and the differenced (CTL - DPV) radial flows (contoured at intervals of 0.2 m s^{-1}); and (c) as in (b), but for the differenced (CTL - HVX) radial flows. In-plane flow vectors show the full secondary circulation for each experiment.

$$q_i = A_1 \sin\left(\frac{\pi z}{H_e}\right) \exp\left[-\left(\frac{z}{H_e}\right)^{\alpha_e}\right] \exp\left[-\left(\frac{r - r_e}{R_e}\right)^2\right], \tag{11a}$$

$$q_o = A_1 \sin\left(\frac{\pi z}{H_e}\right) \exp\left[-\left(\frac{z}{H_e}\right)^{\alpha_e}\right] \exp\left[-\left(\frac{r - r_o}{R_e}\right)^2\right], \tag{11b}$$

where $r_o = 120 \text{ km}$ is the central radius of the outer eyewall at the surface, and all the other parameters have the same physical meaning as q_e in the CTL case, with the peak amplitude of $A_1 = 10 \text{ PVU}$ and a diabatic heating rate of $Q_i = 30 \text{ K h}^{-1}$. These values are based on the

magnitude of the simulated PVA and heating rate associated with the outer eyewall of Bonnie during its eyewall replacement phase. The vertical tilt of the eyewalls is specified by letting the radii of their peak PVAs slope linearly outward according to

$$r = r_o + \alpha z, \tag{12}$$

where α is the slope of the vertical tilt; see Table 1 for more details. Homogeneous boundary conditions are also assumed for both q_o and q_i .

Figure 7 shows the horizontal distribution of pressure perturbations and tangential flows associated with q_o at three selected levels, in which its interactions with the mean vortex and q_i are included as described in section 3. The q_i -induced perturbations are not shown since they are similar to those given in Figs. 3b and 3e, except for its interaction with q_o . First of all, the outer eyewall also induces a balanced low pressure volume within a radius of about 180 km , with a surface low of 10 hPa in the hurricane center and a surface low pressure ring in the outer eyewall. Corresponding to this low pressure volume is a deep layer of cyclonic perturbation flows outside the outer eyewall, which is similar to that shown in Fig. 3b. Of importance is that the q_o -induced flows inside the outer eyewall are anticyclonic with respect to the inner eyewall. As a result, a secondary RMW tends to develop at the outer edge of the outer PVA ring as the outer eyewall wraps around the inner eyewall and contracts radially inward, while the original inner RMW would diminish. This could help explain why two RMWs often coexist during the eyewall replacement period (e.g., see Figs. 14 and 18 in Zhu et al. 2004). Apparently, the stronger the outer eyewall is, the more intense is the surface central pressure, and the stronger (weaker) is the tangential wind outside the outer (inner) eyewall.

It should be noted that although the magnitudes of such anticyclonic perturbation flows induced by the outer eyewall may appear at first relatively weak compared to the mean flows, they are dynamically persistent and will last as long as the double eyewall configuration is maintained. Because of the balanced impact, the mean cyclonic flows will experience continuous deceleration in the vicinity of the moat area during the eyewall replacement cycle. As one could imagine, such inimical impacts could also be held for any closed rainband, or more or less spiral rainbands.

Like the q_o -induced pressure perturbation, its θ' shows a widespread area ($r \sim 180 \text{ km}$) of warming aloft and cooling below, with a peak warm anomaly ring above at the inner edge of the outer eyewall and a weaker warm anomaly centered in the eye (cf. Figs. 8 and 3e), which are hydrostatically consistent with the pressure perturbation

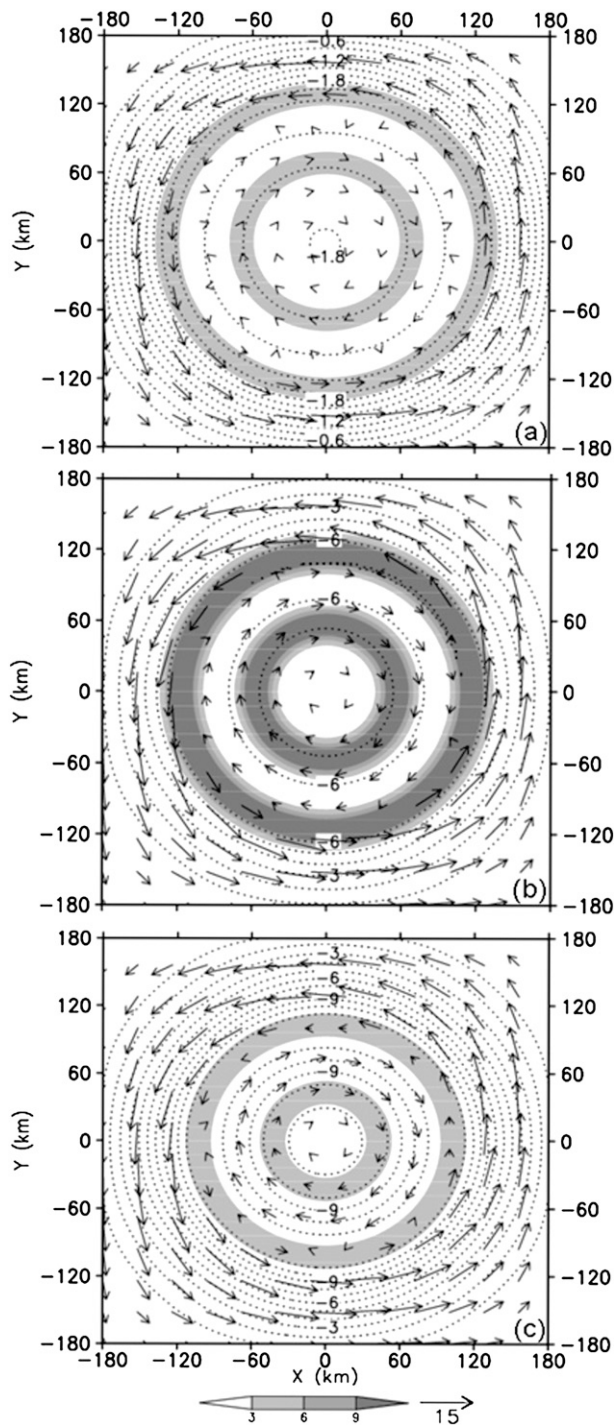


FIG. 7. Horizontal distribution of the negative perturbation pressure (contoured) associated with the outer PVA piece q_o (shaded at intervals of 3 PVU) at $z =$ (a) 10, (b) 3, and (c) 0.5 km. The perturbation pressures are dashed at intervals of 0.2 hPa in (a), and 1 hPa in (b) and (c). Superimposed are the q_o -induced perturbation tangential flows (m s^{-1}).

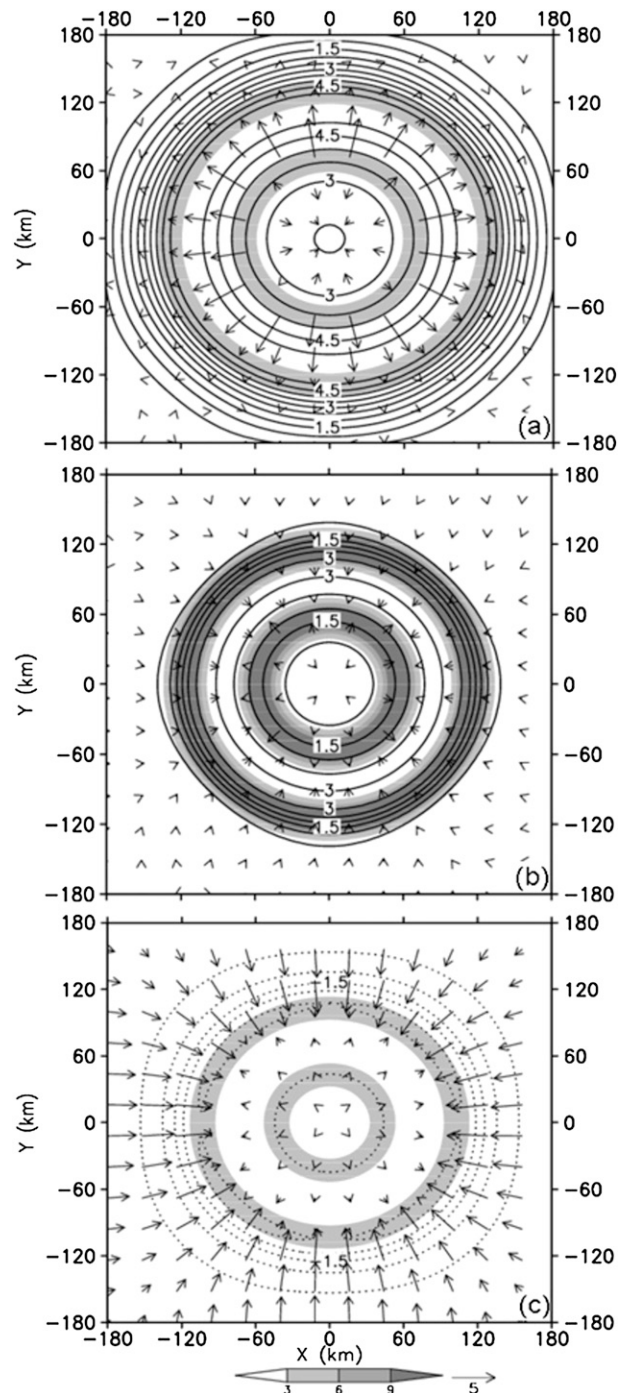


FIG. 8. As in Fig. 7, but for the perturbation potential temperature at intervals of 0.5°C , superimposed with the quasi-balanced divergent flows induced by diabatic heating in the outer eyewall.

field (cf. Figs. 7 and 8). As the lower pressure and thermal anomaly rings are superimposed to those associated with the pre-existing inner eyewall, the radial pressure and thermal gradients may be reduced or even

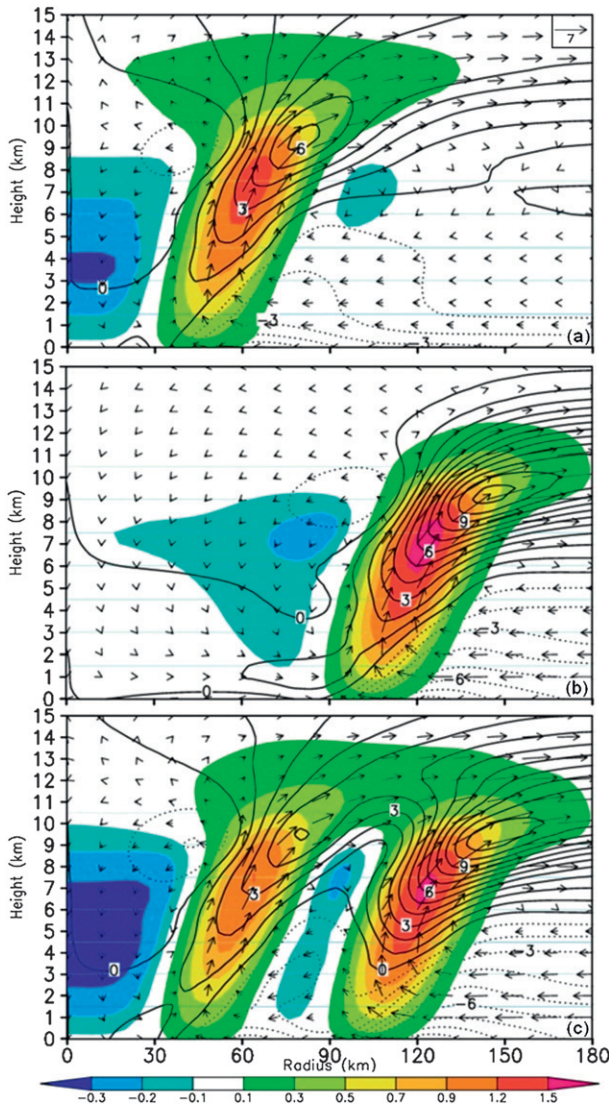


FIG. 9. R - z cross sections of the quasi-balanced vertical motion (shaded, m s^{-1}) and radial flows (contoured at intervals of 0.5 m s^{-1}), superposed with the resultant in-plane flow vectors, associated with (a) Q_i , (b) Q_o , and (c) $Q_i + Q_o$.

reversed between the two eyewalls, thereby reducing the vertical shear of tangential winds in the inner eyewall.

Previous studies have suggested that the outer eyewall not only acts to reduce the lower-level convergence for maintaining deep convection in the inner eyewall but also induces subsidence over the regions occupied by the inner eyewall (Black and Willoughby 1992; Wang 2009). To verify this hypothesis, three PV- ω inversions are performed to estimate the quasi-balanced secondary circulations induced by an inner eyewall (Fig. 9a), an outer eyewall (Fig. 9b), and double eyewalls (Fig. 9c), in which idealized concentric diabatic heating rings (i.e., Q_o and Q_i) collocated with the PVA rings given by Eq. (11)

are superimposed to the mean vortex, with the heating rate chosen in the same manner as in CTL. Although the inner Q_i -induced secondary circulation is similar to the CTL one (cf. Figs. 9a and 6a), its interaction with the q_o -induced balance flows results in weaker inflows in the lowest 5-km layer, especially outside the outer eyewall. Moreover, the blocking of the Q_i -induced upper outflow by the outer eyewall induces weak descent outside the inner eyewall, which is not evident in CTL.

By comparison, the Q_o -induced radial and upward flows are stronger than the Q_i -induced (cf. Figs. 9a,b) because of the presence of weaker inertial stability and weaker static stability outside the outer eyewall than those inside (see also HVX in section 4). Of interest is the Q_o -induced subsidence occurring mostly between the inner edges of the two eyewalls with a peak amplitude up to 0.2 m s^{-1} at the outer edge of the inner eyewall (i.e., near $r = 70 \text{ km}$; Fig. 9b). There is little Q_o -induced subsidence in the eye region because of the blocking of the q_i -induced balance flow. Unlike the analytical model of Rozoff et al. (2008) producing negligible outer-eyewall-induced subsidence in the inner-core region, Fig. 8 shows clearly such subsidence at the magnitudes of 0.1 – 0.2 m s^{-1} with the peak along the inner edge of the outer eyewall. Furthermore, we can see that the Q_o -induced low-level (upper-level) convergence (divergence) could produce an outward (inward) flow component to offset the PBL convergence (divergence) associated with the inner eyewall, which is not captured by Rozoff et al.'s model. Such discrepancies between Rozoff et al.'s and our results could be attributed to their idealized barotropic model in which a radial constant static stability is used. Apparently, in our case, such unrealistic restrictions are not present, thus giving rise to intricate behaviors of the Q_o -induced transverse circulations as seen in Figs. 8 and 9. It follows that the formation of an outer eyewall will be inimical to convective development in the inner eyewall through the reduction of mass and moisture convergence and direct subsidence within the inner eyewall, as previously hypothesized.

When both Q_i - and Q_o -induced secondary circulations are allowed to interact, more pronounced subsidence occurs between the two eyewalls (Fig. 9c), which would clearly favor the formation of a narrow moat area in between. Furthermore, note the significant reduction of the upper-level outflow and the low-level inflow in the inner eyewall under the influence of the Q_o -induced secondary circulation (cf. Figs. 9a,c and 8). In contrast, deep convection in the inner eyewall has little effect on vertical circulations associated with the outer eyewall except for the subsidence inside. Evidently, this result has some important implications to the formation of a moat area between the eyewall and spiral rainbands,

and the suppression of eyewall convection by spiral rainbands. In this regard, the development of spiral rainbands is unfavorable for deep convection in the eyewall.

As the energy supply to the inner eyewall is reduced because of the blocking effects of the outer eyewall, deep convection in the inner (outer) eyewall will weaken (intensify) with time, leading to expansion of the warm core, shift of the RMW to the outer eyewall, and completion of a replacement cycle. Because diabatic heating in the outer eyewall is less efficient than that in the inner eyewall in deepening the hurricane vortex (Hack and Schubert 1986), the surface central pressure and the maximum surface wind may weaken during the eyewall replacement period.

6. Summary and conclusions

In this study, a piecewise PV inversion algorithm for an arbitrary number of PV pieces is presented, and it is then used to examine the nonlinear balanced flows corresponding to various types and intensities of PVAs in hurricane vortices, including those in the eye and eyewall as well as double eyewalls. The PVA-induced balance flows under different background rotations as well as their associated quasi-balanced secondary circulations for a given diabatic heating rate in the eyewalls are also examined.

Results show that each PVA in a hurricane can induce a cyclonic rotation around it with a warm core above a cold dome and a pressure deficit at the bottom of the PVA, which is consistent with those in the previous studies of MCSs (e.g., Raymond and Jiang 1990). It is found that the upper- and lower-level PVAs in the eye help enhance cyclonic flows in the eyewall but exhibit weak vertical interactions. Unlike the previous findings with weaker background rotation, the upper PVA within the hurricane core contributes little to the surface development. Moreover, the quasi-balanced response to latent heat release in the eyewall could account partly for the usually observed warm core in the eye and the minimum central pressure whereas the lower-level PVA in the eye inversion layer appears to contribute more effectively to the hurricane intensity.

Sensitivity experiments with different background vortex strengths show that the radial influence of a PVA is more sensitive to the mean vortex intensity than the vertical penetration. The weaker the background vortex, the larger the radial influence and the stronger the balanced responses will be. The quasi-balanced dynamics shows further that a weaker background vortex tends to enhance the secondary circulation because of the presence of weaker inertial and static stabilities. Similarly, increasing the magnitude of PVAs would allow weaker

secondary circulations to develop. The results suggest that weak vortices are more susceptible to changes induced by any PVA ring in the inner-core regions whereas vortices of greater strength are more resilient to such alterations.

By idealizing the outer eyewall as a ring of PVA, we demonstrated that the development of an outer eyewall could affect the dynamics and evolution of the inner eyewall in several ways. First, the outer eyewall tends to induce a cyclonic flow outside and an anticyclonic flow inside with respect to the inner eyewall, thereby weakening (enhancing) the rotation of the inner (outer) eyewall. This will allow local wind maxima to appear at dual radii during the eyewall replacement period and then shift the RMW outside the outer eyewall as the inner eyewall diminishes. Second, as a ring of a lower pressure associated with the outer eyewall is superimposed on the pre-existing low-pressure volume, the inner-core lower pressure region will be broadened and the radial pressure gradient will be reduced. This would weaken the radial inflow and the inward convergence of absolute angular momentum and energy supply to the inner eyewall. Third, the quasi-balanced dynamics shows that the outer eyewall will induce an inward (outward) radial flow outside (inside) the PBL to block the energy supply to the inner eyewall, and an outward (weak inward) radial flow outside (inside) in the upper layers, leading to the development of subsidence between the two eyewalls. This will not only widen the moat area between the two eyewalls but also suppress deep convection in the inner eyewall. This result appears to have important implications for the development of moat areas between spiral rainbands and the eyewall. Thus, we may conclude that the generation of an outer eyewall (or spiral rainbands) is inimical to the development of deep convection in the inner eyewall and the intensification of hurricanes. It should be emphasized, however, that although the formation of spiral bands and their subsequent wrapping around may act to affect an inner eyewall in some causal sense, our results are restricted within the PV- ω diagnostic framework only.

Acknowledgments. We thank Dr. Chris Davis and two anonymous reviewers for their constructive comments, and Dr. Walt Robinson for his editorial comments. This work was supported by NSF Grant ATM-0758609, NASA Grant NNG05GR32G, and ONR Grant N000140710186.

REFERENCES

- Bell, M. M., and M. T. Montgomery, 2008: Observed structure, evolution, and potential intensity of Category 5 Hurricane Isabel (2003) from 12 to 14 September. *Mon. Wea. Rev.*, **136**, 2023–2046.

- Black, M. L., and H. E. Willoughby, 1992: The concentric eyewall cycle of Hurricane Gilbert. *Mon. Wea. Rev.*, **120**, 947–957.
- Blackwell, K. G., 2000: The evolution of Hurricane Danny (1997) at landfall: Doppler-observed eyewall replacement, vortex contraction/intensification, and low-level wind maxima. *Mon. Wea. Rev.*, **128**, 4002–4016.
- Chen, Y., and M. K. Yau, 2001: Spiral bands in a simulated hurricane. Part I: Vortex Rossby wave verification. *J. Atmos. Sci.*, **58**, 2128–2145.
- Davis, C. A., 1992: Piecewise potential vorticity inversion. *J. Atmos. Sci.*, **49**, 1397–1411.
- , and K. Emanuel, 1991: Potential vorticity diagnostics of cyclogenesis. *Mon. Wea. Rev.*, **119**, 1929–1953.
- Egger, J., 2008: Piecewise potential vorticity inversion: Elementary tests. *J. Atmos. Sci.*, **65**, 2015–2024.
- Eliassen, A., 1952: Slow thermally or frictionally controlled meridional circulation in a circular vortex. *Astrophys. Norv.*, **5**, 19–60.
- Guinn, T. A., and W. H. Schubert, 1993: Hurricane spiral bands. *J. Atmos. Sci.*, **50**, 3380–3403.
- Hack, J. J., and W. H. Schubert, 1986: Nonlinear response of atmospheric vortices to heating by organized cumulus convection. *J. Atmos. Sci.*, **43**, 1559–1573.
- Hoskins, B. J., and F. P. Bretherton, 1972: Atmospheric frontogenesis models: Mathematical formulation and solution. *J. Atmos. Sci.*, **29**, 11–37.
- , M. E. McIntyre, and A. W. Robertson, 1985: On the use and significance of isentropic potential vorticity maps. *Quart. J. Roy. Meteor. Soc.*, **111**, 877–946.
- Huo, Z., D.-L. Zhang, and J. R. Gyakum, 1998: An application of potential vorticity inversion to improving the numerical prediction of the March 1993 superstorm. *Mon. Wea. Rev.*, **126**, 424–436.
- , —, and —, 1999: Interaction of potential vorticity anomalies in extratropical cyclogenesis. Part I: Static piecewise inversion. *Mon. Wea. Rev.*, **127**, 2546–2562.
- Kossin, J. P., W. H. Schubert, and M. T. Montgomery, 2000: Unstable interactions between a hurricane's primary eyewall and a secondary ring of enhanced vorticity. *J. Atmos. Sci.*, **24**, 3893–3917.
- Liu, Y., D.-L. Zhang, and M. K. Yau, 1999: A multiscale numerical study of Hurricane Andrew (1992). Part II: Kinematics and inner-core structures. *Mon. Wea. Rev.*, **127**, 2597–2616.
- McNoldy, B. D., 2004: Triple eyewall in Hurricane Juliette. *Bull. Amer. Meteor. Soc.*, **85**, 1663–1666.
- Raymond, D. J., and H. Jiang, 1990: A theory for long-lived mesoscale convective systems. *J. Atmos. Sci.*, **47**, 3067–3077.
- Rossby, C. G., 1940: Planetary flow patterns in the atmosphere. *Quart. J. Roy. Meteor. Soc.*, **66**, 68–87.
- Rozoff, C. M., W. H. Schubert, and J. P. Kossin, 2008: Some dynamical aspects of tropical cyclone concentric eyewalls. *Quart. J. Roy. Meteor. Soc.*, **134**, 583–593.
- Shapiro, L. J., and J. D. Möller, 2003: Influence of atmospheric asymmetries on the intensification of Hurricane Opal: Piecewise PV inversion diagnosis of a GFDL model forecast. *Mon. Wea. Rev.*, **131**, 1637–1649.
- Wang, X., and D.-L. Zhang, 2003: Potential vorticity diagnosis of a simulated hurricane. Part I: Formulation and quasi-balanced flow. *J. Atmos. Sci.*, **60**, 1593–1607.
- Wang, Y., 2008: Rapid filamentation zone in a numerically simulated tropical cyclone. *J. Atmos. Sci.*, **65**, 1158–1181.
- , 2009: How do outer spiral rainbands affect tropical cyclone structure and intensity? *J. Atmos. Sci.*, **66**, 1250–1273.
- Willoughby, H. E., J. A. Clos, and M. G. Shoreibah, 1982: Concentric eyewalls, secondary wind maxima, and the evolution of the hurricane vortex. *J. Atmos. Sci.*, **39**, 395–411.
- , F. D. Marks, and R. J. Feinberg, 1984: Stationary and moving convective bands in hurricanes. *J. Atmos. Sci.*, **41**, 3189–3211.
- Wu, C.-C., and K. A. Emanuel, 1995a: Potential vorticity diagnostics of hurricane movement. Part I: A case study of Hurricane Bob (1991). *Mon. Wea. Rev.*, **123**, 69–92.
- , and —, 1995b: Potential vorticity diagnostics of hurricane movement. Part II: Tropical Storm Ana (1991) and Hurricane Andrew (1992). *Mon. Wea. Rev.*, **123**, 93–109.
- Yau, M. K., Y. Liu, D.-L. Zhang, and Y. Chen, 2004: A multiscale numerical study of Hurricane Andrew (1992). Part VI: Small-scale inner-core structures and wind streaks. *Mon. Wea. Rev.*, **132**, 1410–1433.
- Zhang, D.-L., and C. Q. Kieu, 2006: Potential vorticity diagnosis of a simulated hurricane. Part II: Quasi-balanced contributions to forced secondary circulations. *J. Atmos. Sci.*, **63**, 2898–2914.
- , Y. Liu, and M. K. Yau, 2001: A multiscale numerical study of Hurricane Andrew (1992). Part IV: Unbalanced flows. *Mon. Wea. Rev.*, **129**, 92–107.
- , —, and —, 2002: A multiscale numerical study of Hurricane Andrew (1992). Part V: Inner-core thermodynamics. *Mon. Wea. Rev.*, **130**, 2745–2763.
- Zhu, T., D.-L. Zhang, and F. Weng, 2004: Numerical simulation of Hurricane Bonnie (1998). Part I: Eyewall evolution and intensity changes. *Mon. Wea. Rev.*, **132**, 225–241.